

## ORIGINAL RESEARCH

# Disturbance-rejection adjacent vector model predictive control strategy based on extended state observer for EV converter

Jianwei Zhang<sup>1</sup>  | Qiaosen Cao<sup>1</sup> | Guangchen Liu<sup>1</sup> | Marco Rivera<sup>2</sup> | Patrick Wheeler<sup>2</sup>

<sup>1</sup>College of Electric Power, Inner Mongolia University of Technology, Hohhot, China

<sup>2</sup>PEMC Group, Faculty of Engineering, University of Nottingham, Nottingham, UK

## Correspondence

Jianwei Zhang, College of Electric Power, Inner Mongolia University of Technology, Hohhot 010080, China.

Email: zjwzachary@outlook.com

## Funding information

Program for Young Talents of Science and Technology in Universities of Inner Mongolia Autonomous Region, Grant/Award Number: NJYT22082; Basic Scientific Research Expenses Program of Universities directly under Inner Mongolia Autonomous Region, Grant/Award Numbers: JY20220092, JY20230009; University of Nottingham International Research Collaboration Fund, Grant/Award Number: A71502; Fondecyt Regular Project, Grant/Award Number: 1220556; Anid/Anillo Project, Grant/Award Number: ATE220023; FONDAP SERC Chile, Grant/Award Number: 1522A0006; Inner Mongolia Natural Science Foundation, Grant/Award Number: 2024MS05041; Inner Mongolia Autonomous Region Science and Technology Breakthrough, Grant/Award Number: 2024KJTW0017

## Abstract

Conventional single-vector model predictive control (MPC) can suffer from low control accuracy, while multi-vector MPC is often criticized for its complexity and heavy computational burden. In order to address these issues, an adjacent vector-based MPC is investigated in this paper for an electric vehicle battery charging and discharging converter. The voltage vector selection table based on the principle of using adjacent vectors has been designed and this reduces the number of iterations and thus the computational burden. A threshold is used in the adjacent vector-based MPC to coordinate the use of the single and multi-vector MPCs considering a balance between the control accuracy and computational burden. In addition, to enhance the robustness of MPC to parameter changes, an extended state observer for active disturbance rejection control has been used to derive the predictive model, and an adjacent vector-based MPC using extended state observer is studied. The method does not need accurate system parameters. Instead, it only requires the system input and output measurements to calculate the predicted current. The robustness of the controller against the parameter mismatch is enhanced compared to alternative approaches and the experimental results verify the feasibility and effectiveness of the proposed strategy.

## 1 | INTRODUCTION

Model predictive control (MPC) has been widely researched for power electronic converters due to its advantages including fast dynamic response, easiness in understanding, simplicity in implementation, no modulation stage, flexibility in realizing multi-objective control and including system constraints [1, 2]. However, there are some issues associated with the MPC, such as dependence on system parameters, variable switching frequency, heavy computational burden in some cases, and difficult weighting factor tuning. In addition, MPC is sometimes criticized for issues such as difficulty in balancing the control accuracy and computational burden and dependence on sys-

tem parameters [3, 4]. The balance of the control accuracy and computational burden is the main concern of this paper.

Traditional single-vector MPC (or 1-vector MPC) only applies one switch state in each control period. Hence, the control performance is not always guaranteed under certain conditions [5, 6]. Large current and power ripples, noticeable steady-state error and low control accuracy in 1-vector MPC have been reported [7]. Therefore, various multi-vector MPC schemes have been proposed in the literature [8–10]. Double-vector (or 2-vector) MPC uses two voltage vectors to synthesize the reference vector in one sampling period, which can improve control accuracy at the cost of increased complexity and computational burden [11]. Three-vector (or 3-vector) MPC uses

This is an open access article under the terms of the [Creative Commons Attribution](https://creativecommons.org/licenses/by/4.0/) License, which permits use, distribution and reproduction in any medium, provided the original work is properly cited.

© 2024 The Author(s). *IET Power Electronics* published by John Wiley & Sons Ltd on behalf of The Institution of Engineering and Technology.

two non-zero voltage vectors and one zero-voltage vector in one sampling period. Theoretically, any desired bridge arm voltage vectors can be formed, thus achieving dead-beat control accuracy [12, 13]. However, the computational burden is further increased. Although the multi-vector MPC can improve the control accuracy, it is computationally extensive because of enumeration-based iterative calculations [14]. An adjacent vector-based MPC (AVB-MPC) strategy that coordinates the application of 1-vector, 2-vector, and 3-vector schemes has been studied for motor drives in [15]. However, the calculation of the duty cycle is rather complicated, and it increases the computational burden. However, a strategy with high control accuracy and reasonable computational burden is desired in the field of MPC. Based on the above analysis, this paper investigates an AVB-MPC for EV converter to improve control accuracy while maintaining a low computational burden.

Another challenge MPC faces is the dependence on system parameters which may change under different operating conditions. Inaccurate system parameters may lead to deteriorated or even unsatisfactory performance [16, 17]. Some strategies have been proposed in the literature to reduce the dependence of the MPC on system parameters and a review can be found in [18]. Model-free MPC based on the extended state observer (ESO) has been widely studied recently to address the parametric uncertainties [19, 20]. In [15], the full model estimation method has been proposed to eliminate the influence of parameter errors. However, possible rank deficiency issues may affect estimation performance. In [21], an ESO based on an ultralocal model has been proposed to achieve model-free MPC. However, the bandwidth performance of these methods cannot be further improved due to missing model information [22]. Cascaded ESOs and relevant derivatives have also been investigated for MPC; nevertheless, these methods are either complex or require extensive computations. There is a lack of a generalized design procedure for the MPC of power converters based on ESO in the literature.

The control performance of MPC relies on the accuracy of model parameters. However, the model parameters may change under different working conditions or different environments, resulting in an inaccurate predictive model and thus deteriorated control performance. In this paper, inspired by active disturbance control (ADRC) [23], a disturbance-rejection predictive model has been investigated from a different perspective. ADRC is a model-free control technique that uses an extended state observer (ESO) to estimate the system's unknown dynamics and disturbances. Based on this characteristic, a disturbance-rejection predictive model is built in which the system parameter inaccuracy is regarded as part of the disturbance and estimated by ESO, thus reducing the dependence of the controller on system parameters. With the integration of ESO into the MPC, the predicted current can be obtained without an accurate system model, thus improving the parameter robustness.

The main contents of this paper are summarized as follows. (1) An AVB-MPC with a control error threshold is investigated to coordinate the use of 1-vector, 2-vector and 3-vector MPC methods, thus improving the control accuracy and maintaining

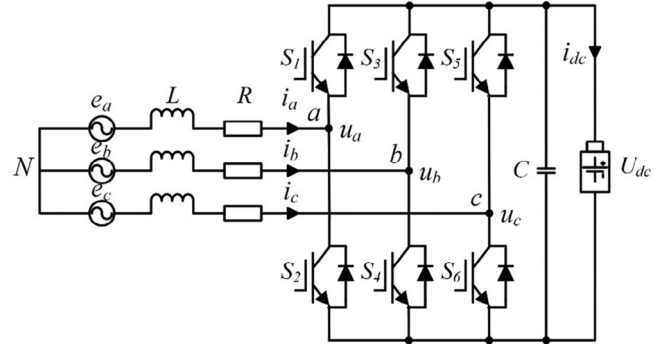


FIGURE 1 Topology of EV battery charging and discharging converter.

a low computational burden. (2) A vector selection table based on the principle of using adjacent vectors and minimum switching is utilized, which helps reduce the computational burden and switching frequency. (3) Inspired by ADRC, a disturbance-rejection predictive model is developed based on ESO to reduce the dependence of the controller on system parameters. The AVB-MPC is combined with the predictive model based on ESO to enhance the overall performance. The proposed method combines AVB-MPC with ESO and it only requires input and output data of the system, rather than accurate system parameters. A generalized design procedure for a predictive model based on ESO is presented to facilitate extending the method for other power electronic converters. Experimental results obtained on an electric vehicle (EV) battery charging and discharging converter verify the effectiveness of the proposed strategies.

## 2 | AVB-MPC PRINCIPLE

### 2.1 | Traditional MPC

The EV battery charging and discharging converter is shown in Figure 1. According to Kirchhoff's voltage law (KVL), the AC-side system model in the  $dq$  rotating coordinate system is

$$\begin{cases} \frac{di_d}{dt} = \frac{e_d}{L} - \frac{u_d}{L} - \frac{R}{L}i_d + \omega i_q \\ \frac{di_q}{dt} = \frac{e_q}{L} - \frac{u_q}{L} - \frac{R}{L}i_q - \omega i_d \end{cases} \quad (1)$$

where  $i_{d,q}$  and  $e_{d,q}$  are the  $d$ - and  $q$ -axis components of the grid current and voltage;  $u_{d,q}$  are the  $d$ - and  $q$ -axis components of converter voltage;  $L$  and  $R$  are inductance and resistance;  $\omega$  is the angular frequency. By discretizing Equation (1), the current predictive model can be derived,

$$\begin{cases} i_d(k+1) = \frac{T_s}{L} [e_d(k) - u_d(k) - Ri_d(k) + \omega i_q] + i_d(k) \\ i_q(k+1) = \frac{T_s}{L} [e_q(k) - u_q(k) - Ri_q(k) - \omega i_d] + i_q(k) \end{cases} \quad (2)$$

**TABLE 1** AVB-MPC voltage vector selection table.

Last applied vector $u_0$	1-vector scheme	2-vector scheme	3-vector scheme					
			Sector number of the reference voltage					
			I	II	III	IV	V	VI
$u_1$	$u_1$	$(u_1, u_3), (u_1, u_2), (u_1, u_4)$	$(u_1, u_2, u_5)$	$(u_1, u_3, u_5)$	$(u_1, u_3, u_7)$	$(u_1, u_4, u_7)$	$(u_1, u_4, u_6)$	$(u_1, u_2, u_6)$
$u_2$	$u_2$	$(u_2, u_5), (u_2, u_1), (u_2, u_6)$	$(u_2, u_5, u_8)$	$(u_5, u_3, u_1)$	$(u_1, u_3, u_7)$	$(u_1, u_4, u_7)$	$(u_6, u_4, u_1)$	$(u_2, u_6, u_8)$
$u_3$	$u_3$	$(u_3, u_5), (u_3, u_7), (u_3, u_1)$	$(u_5, u_2, u_1)$	$(u_3, u_5, u_8)$	$(u_3, u_7, u_8)$	$(u_7, u_4, u_1)$	$(u_1, u_4, u_6)$	$(u_1, u_2, u_6)$
$u_4$	$u_4$	$(u_4, u_7), (u_4, u_6), (u_4, u_1)$	$(u_1, u_2, u_5)$	$(u_1, u_3, u_5)$	$(u_7, u_3, u_1)$	$(u_4, u_7, u_8)$	$(u_4, u_8, u_6)$	$(u_6, u_2, u_1)$
$u_5$	$u_5$	$(u_5, u_2), (u_5, u_3), (u_5, u_8)$	$(u_5, u_2, u_1)$	$(u_5, u_3, u_1)$	$(u_3, u_7, u_8)$	$(u_8, u_7, u_4)$	$(u_8, u_6, u_4)$	$(u_2, u_6, u_8)$
$u_6$	$u_6$	$(u_6, u_2), (u_6, u_4), (u_6, u_8)$	$(u_2, u_5, u_8)$	$(u_8, u_5, u_3)$	$(u_8, u_7, u_3)$	$(u_4, u_7, u_8)$	$(u_6, u_4, u_1)$	$(u_6, u_2, u_1)$
$u_7$	$u_7$	$(u_7, u_3), (u_7, u_4), (u_7, u_8)$	$(u_8, u_5, u_2)$	$(u_3, u_5, u_8)$	$(u_7, u_3, u_1)$	$(u_7, u_4, u_1)$	$(u_4, u_6, u_8)$	$(u_8, u_6, u_2)$
$u_8$	$u_8$	$(u_8, u_6), (u_8, u_5), (u_8, u_7)$	$(u_8, u_5, u_2)$	$(u_8, u_5, u_3)$	$(u_8, u_7, u_3)$	$(u_8, u_7, u_4)$	$(u_8, u_6, u_4)$	$(u_8, u_6, u_2)$

where  $T_s$  represents the sampling time. As observed in Equation (2), inaccurate parameter values can lead to inaccurate predicted current values, thus deteriorating the control performance.

MPC uses a cost function to evaluate the impact of each switching state on the predicted current, so as to select the switching state that minimizes the cost function. The cost function is

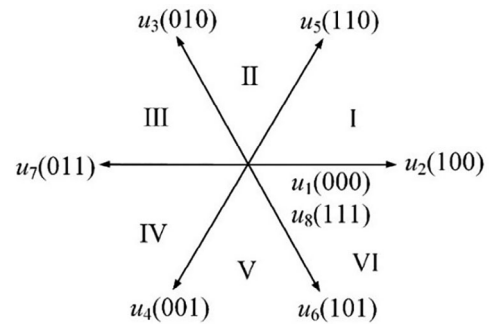
$$g = [i_d^* - i_d(k+1)]^2 + [i_q^* - i_q(k+1)]^2 \quad (3)$$

where  $i_d^*$  and  $i_q^*$  are the corresponding references. In the traditional multi-vector MPC, all switching state combinations are considered in the predictive model and evaluated by the cost function. Therefore, the computational burden is remarkably increased.

## 2.2 | Vector selection table

The AVB-MPC strategy uses a predefined voltage vector selection table that is designed based on the principle of using adjacent vectors to select the switching state candidate or combinations. Pre-selection of switching states can eliminate the switching states that are unlikely to be applied and therefore help reduce the computational burden effectively. The designed voltage vector selection table is shown in Table 1.

Based on the voltage vector diagram shown in Figure 2, the design of Table 1 is explained. Assume that the voltage vector applied in the last control interval is  $u_2$  (100). In the 1-vector scheme,  $u_2$  is still selected with the principle of the minimum switching of switches. In the 2-vector scheme, four 2-vector combinations, namely  $(u_2, u_5)$ ,  $(u_2, u_6)$ ,  $(u_2, u_8)$ , and  $(u_2$  and  $u_1)$  are considered based on the principle of using adjacent vectors and zero vectors. The  $(u_2, u_8)$  combination can be removed because it causes more switching actions. In the 3-vector scheme, the reference voltage vector and its location can be obtained using Equation (2) based on the dead-beat control theory. If the reference voltage vector is located in sector III, the possible 3-vector combinations are  $u_3$  (010),  $u_7$  (011),  $u_1$  (000)

**FIGURE 2** Voltage vector diagram.

or  $u_3$  (010),  $u_7$  (011),  $u_8$  (111). If the voltage vector at the end of the last cycle is  $u_2$  (100), the 3-vector combination should be  $(u_1, u_3, u_7)$  according to the principle of minimum switching. Based on the above analysis, Table 1 can be derived.

## 2.3 | AVB-MPC

In the single-vector method, the control accuracy is low because it is hard to guarantee that the applied vector is the same as the desired vector. Since only one vector is selected and there is no need to calculate the duty cycles, the computational burden of the single-vector scheme is low. In contrast, the control accuracy of the multi-vector scheme is higher because multiple vectors are used to synthesize the desired vector. However, the computational burden is high because the calculation of duty cycles for each vector is required. The simulated turnaround time of the 1-vector, 2-vector, and 3-vector scheme is roughly 57, 90, and 125  $\mu$ s, respectively.

Therefore, a controller that coordinates the use of single-vector and multi-vector schemes is studied in this paper. The AVB-MPC strategy coordinates the selection and application of 1-vector, 2-vector, and 3-vector MPC schemes by comparing the control error with the defined threshold  $C_b$ . When the cost function (control error) is lower than the threshold, the

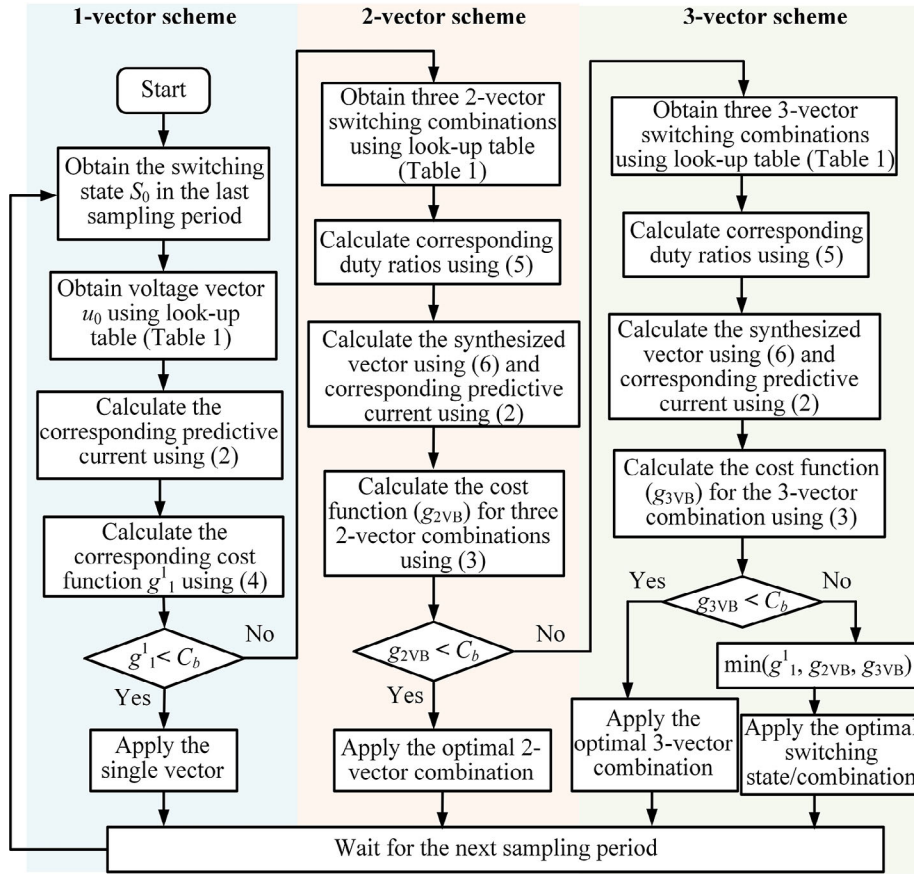


FIGURE 3 AVB-MPC algorithm flowchart.

single-vector scheme is employed. When the control error is larger than the threshold, the multi-vector scheme is adopted. Therefore, the threshold coordinates the use of single-vector and multi-vector schemes and it helps balance the control accuracy and computational burden. The flow chart of the AVB-MPC scheme is shown in Figure 3.

The control procedure is arranged as follows:

1) **1-vector scheme**

In the 1-vector scheme, the vector applied in the last control cycle is evaluated. If the control error (calculated by the cost function using Equation (3) or (4)) caused by 1-vector MPC is less than  $C_b$ , then 1-vector MPC is adopted; otherwise, the 2-vector MPC is considered.

2) **2-vector scheme**

In the 2-vector scheme, 2-vector combinations shown in Table 1 are evaluated. Firstly, cost functions for vectors in each 2-vector combination are calculated using Equation (3). To facilitate analysis and explanation, Equation (3) can be generalized as

$$g_n^m = [i_d^* - i_{dn}^m(k+1)]^2 + [i_q^* - i_{qn}^m(k+1)]^2 \quad (4)$$

where  $g_n^m$  is the cost function value corresponding to the  $m$ th vector in the  $n$ -vector combination ( $m \leq n$  and  $n = 1, 2$  or  $3$ );  $i_{dn}^m(k+1)$ ,  $i_{qn}^m(k+1)$  are the predicted current corresponding to the  $m$ th vector in the  $n$ -vector combination.

In the multi-vector control strategy, the candidate vectors are used to synthesize the desired vector. Therefore, the corresponding action time (or duty ratios) of each vector should be determined. The action time of each voltage vector in multi-vector control is inversely proportional to its corresponding cost function value [7]. That is to say, the larger the cost function value, the shorter the action time to be applied (because of less control accuracy). Therefore, the action time of the  $m$ th vector in  $n$ -vector control can be calculated by

$$t_n^m = \frac{\frac{1}{g_n^m}}{\frac{1}{g_n^1} + \dots + \frac{1}{g_n^n}} \times T_s \quad (5)$$

where  $T_s$  is the sampling time and  $t_n^1 + \dots + t_n^n = T_s$ . Consequently, the synthesized vector using multi-vector combinations can be expressed by

$$u_n^x = u_n^1 t_n^1 + \dots + u_n^n t_n^n \quad (6)$$

where  $u_n^x$  represents the  $x$ th synthesized vector using  $n$ -vector combination;  $x = 1, 2, 3$  for 2-vector schemes, and 1 for

1-vector and 3-vector schemes. The synthesized vector can then be used to calculate the corresponding predictive current using Equation (2), and the corresponding cost function ( $g_{2VB}$  for the 2-vector scheme and  $g_{3VB}$  for the 3-vector scheme) using Equation (3).

If the control error caused by the optimal 2-vector scheme is less than  $C_b$ , then the optimal 2-vector combination is used; otherwise, the 3-vector scheme is considered.

### 3) 3-vector scheme

In the 3-vector scheme, the 3-vector combination is obtained according to Table 1. Similar to the 2-vector scheme, the cost functions and action times for each vector in the 3-vector combination are calculated using Equations (4) and (5). Then the synthesized vector obtained by the 3-vector combination using Equation (6) is used to derive the predictive current using Equation (2) and the corresponding cost function using Equation (3).

If the control error caused by the 3-vector combination is less than  $C_b$ , then the 3-vector scheme is employed as the optimal scheme; otherwise, the 1-vector, 2-vector, and 3-vector schemes are overall compared, and the control scheme with the minimum control error is eventually adopted.

As concluded from the above analysis, the computational burden is significantly reduced because of the reduced number of switch candidates, thanks to the predefined vector selection table. The control accuracy is also guaranteed since a threshold  $C_b$  is introduced to coordinate the use of 1-vector, 2-vector, and 3-vector schemes, while the computation is not noticeably increased. The design of  $C_b$  can be based on the desired control error depending on specific applications.  $C_b$  affects the control precision and computational burden of the controller. The larger the  $C_b$ , the lower the control precision and the lower the computational burden.

## 3 | AVB-MPC BASED ON ESO

ESO is generally used in ADRC to estimate system disturbance [24]. Inspired by this, ESO is used to obtain the disturbance-rejection predictive model for MPC. A generalized design procedure for designing the predictive model based on ESO is presented as follows.

### 3.1 | ESO principle (generalized approach)

The state-space model of a first-order differential system is expressed by

$$\dot{x} = Ax + Bu \quad (7)$$

$$y = Cx + Du \quad (8)$$

where  $x$  is the state variable;  $u$  is the system input;  $y$  is the system output.  $A$ ,  $B$ ,  $C$ ,  $D$  are state-space matrices. ESO is formed by extending an extra state, i.e. system disturbance.

Let  $x_1 = x$  and  $x_2 = d = Ax$  be the system disturbance and  $\dot{x}_2 = b$ , then Equations (7) and (8) can be rewritten as

$$\dot{X} = \begin{bmatrix} \dot{x}_1 \\ \dot{x}_2 \end{bmatrix} = A' \begin{bmatrix} x_1 \\ x_2 \end{bmatrix} + B' \begin{bmatrix} u \\ b \end{bmatrix} = A'X + B'U \quad (9)$$

$$Y = C' \begin{bmatrix} x_1 \\ x_2 \end{bmatrix} + D' \begin{bmatrix} u \\ b \end{bmatrix} = C'X + D'U \quad (10)$$

with

$$A' = \begin{bmatrix} 0 & 1 \\ 0 & 0 \end{bmatrix}, B' = \begin{bmatrix} 1 & 0 \\ 0 & 1 \end{bmatrix}, C' = [1 \ 0], D' = 0$$

Assume  $\hat{X}$  is the estimated value of the state variable  $X$  and  $\hat{Y}$  is the estimated value of the output  $Y$ , then ESO can be expressed by

$$\dot{\hat{X}} = A'\hat{X} + B'U + G(Y - \hat{Y}) \quad (11)$$

$$\hat{Y} = C'\hat{X} + D'U \quad (12)$$

where  $G$  is the gain matrix of the observer. Substituting Equation (12) into Equation (11) leads to

$$\begin{aligned} \dot{\hat{X}} &= A'\hat{X} + B'U + GY - G(C'\hat{X} + D'U) \\ &= (A' - GC')\hat{X} + (B' - GD')U + GY \end{aligned} \quad (13)$$

According to Equations (9)–(13), one can derive

$$\dot{X} - \dot{\hat{X}} = A'X + B'U - (A' - GC')\hat{X} - (B' - GD')U - GY \quad (14)$$

Substituting (10) into (14) results in

$$\dot{X} - \dot{\hat{X}} = (A' - GC')(X - \hat{X}) \quad (15)$$

If the estimation error is represented by  $e_x = X - \hat{X}$ , then Equation (15) becomes

$$\dot{e}_x = (A' - GC')e_x \quad (16)$$

According to automatic control theory, the necessary and sufficient condition for the equilibrium state ( $e_x = 0$ ) to be asymptotically stable is that the eigenvalues of  $(A' - GC')$  have negative real parts. Therefore, in the design of ESO, one can assume that  $(A' - GC')$  has two same and negative eigenvalues  $-\omega_0$ .

According to the above analysis, ESO can estimate the extended state, i.e. the system disturbance  $d$ . Based on this feature, the MPC model parameter mismatch or inaccuracy is regarded as a system disturbance and estimated by the ESO.

### 3.2 | Predictive model based on ESO

The ESO corresponding to the  $d$ -axis model in Equation (1) is illustrated here and the ESO for the  $q$ -axis model can be obtained using the same way.

The items except for  $u_d$  on the right side of the  $d$ -axis model in Equation (1) are taken as the total system disturbance represented by  $d_d$ , and its derivative is represented by  $b_d$ . Hence, the  $d$ -axis model in Equation (1) can be rewritten as

$$\begin{bmatrix} \dot{i}_d \\ \dot{d}_d \end{bmatrix} = \begin{bmatrix} 0 & 1 \\ 0 & 0 \end{bmatrix} \begin{bmatrix} i_d \\ d_d \end{bmatrix} + \begin{bmatrix} \frac{1}{L} & 0 \\ 0 & 1 \end{bmatrix} \begin{bmatrix} u_d \\ b_d \end{bmatrix} \quad (17)$$

If the gain matrix of ESO for the  $d$ -axis model is  $\mathbf{G} = [G_1 \ G_2]^T$ , then,

$$\left| s\mathbf{I} - (\mathbf{A}' - \mathbf{G}\mathbf{C}') \right| = s^2 + G_1s + G_2 = [s - (-\omega_0)]^2 \quad (18)$$

Therefore, one can derive  $\mathbf{G} = [G_1 \ G_2]^T = [2\omega_0 \ \omega_0^2]^T$ , where  $\omega_0$  is called observer bandwidth. Then ESO for the  $d$ -axis model is

$$\begin{bmatrix} \dot{\hat{i}}_d \\ \dot{\hat{d}}_d \end{bmatrix} = \left\{ \begin{bmatrix} 0 & 1 \\ 0 & 0 \end{bmatrix} - \begin{bmatrix} 2\omega_0 \\ \omega_0^2 \end{bmatrix} \begin{bmatrix} 1 & 0 \end{bmatrix} \right\} \begin{bmatrix} \hat{i}_d \\ \hat{d}_d \end{bmatrix} + \begin{bmatrix} \frac{1}{L} & 2\omega_0 & 0 \\ 0 & \omega_0^2 & 1 \end{bmatrix} \begin{bmatrix} u_d \\ i_d \\ b_d \end{bmatrix} \quad (19)$$

where the derivative of  $d_d$  is

$$b_d = \dot{d}_d = -\frac{\dot{e}_d}{L} - \frac{R}{L}i_d + \omega i_q \quad (20)$$

The  $i_d$  term in  $d_d$  can be incorporated into the state variable matrix. So, Equations (19) and (20) can be restructured as

$$\begin{bmatrix} \dot{\hat{i}}_d \\ \dot{\hat{d}}_d \end{bmatrix} = \left\{ \begin{bmatrix} -\frac{R}{L} & 1 \\ 0 & 0 \end{bmatrix} - \begin{bmatrix} G_1 \\ G_2 \end{bmatrix} \begin{bmatrix} 1 & 0 \end{bmatrix} \right\} \begin{bmatrix} \hat{i}_d \\ \hat{d}_d \end{bmatrix} + \begin{bmatrix} \frac{1}{L} & G_1 & 0 \\ 0 & G_2 & 1 \end{bmatrix} \begin{bmatrix} u_d \\ i_d \\ b_d \end{bmatrix} \quad (21)$$

$$\begin{aligned} b_d = \dot{d}_d &= -\frac{\dot{e}_d}{L} + \omega i_q = \omega \left( \frac{u_q}{L} - \frac{e_q}{L} - \frac{R}{L}i_q - \omega i_d \right) \\ &= -\omega^2 i_d - \frac{R\omega}{L}i_q - \frac{\omega}{L}e_q + \frac{\omega}{L}u_q \end{aligned} \quad (22)$$

where  $\mathbf{G} = [G_1 \ G_2]^T$  is  $[2\omega_0 - R/L \ \omega_0^2]^T$  in this case.

According to Equation (21), the  $d$ -axis current predictive model can be derived

$$i_d(k+1) = \hat{i}_d + T_s \left( -2\omega_0 \hat{i}_d + \hat{d}_d + \frac{1}{L}u_d + 2\omega_0 i_d \right) \quad (23)$$

Similarly, the  $q$ -axis current predictive model can be obtained. The predicted current is obtained by Equation (23) in the disturbance-rejection MPC based on ESO (ESO-MPC). This way, the parameter mismatch or inaccuracy is estimated by ESO as part of the system disturbance, as long as ESO can effectively estimate the system state. Therefore, the robustness of the controller is enhanced with the ESO-MPC strategy.

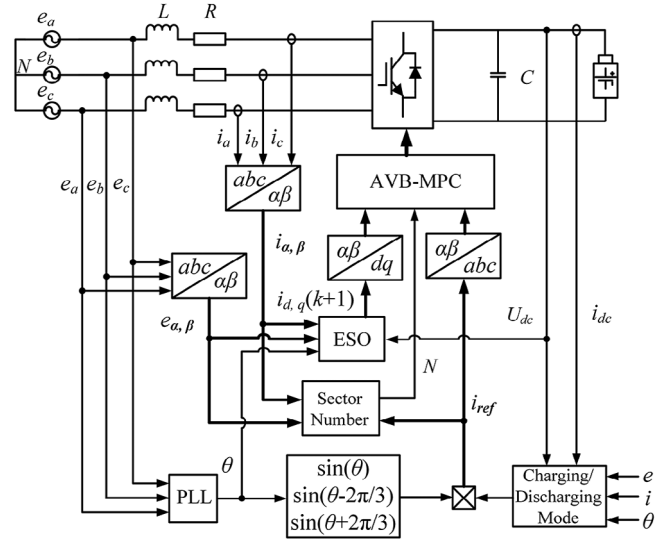


FIGURE 4 ESO-AVB-MPC control block diagram for EV battery charging and discharging system.

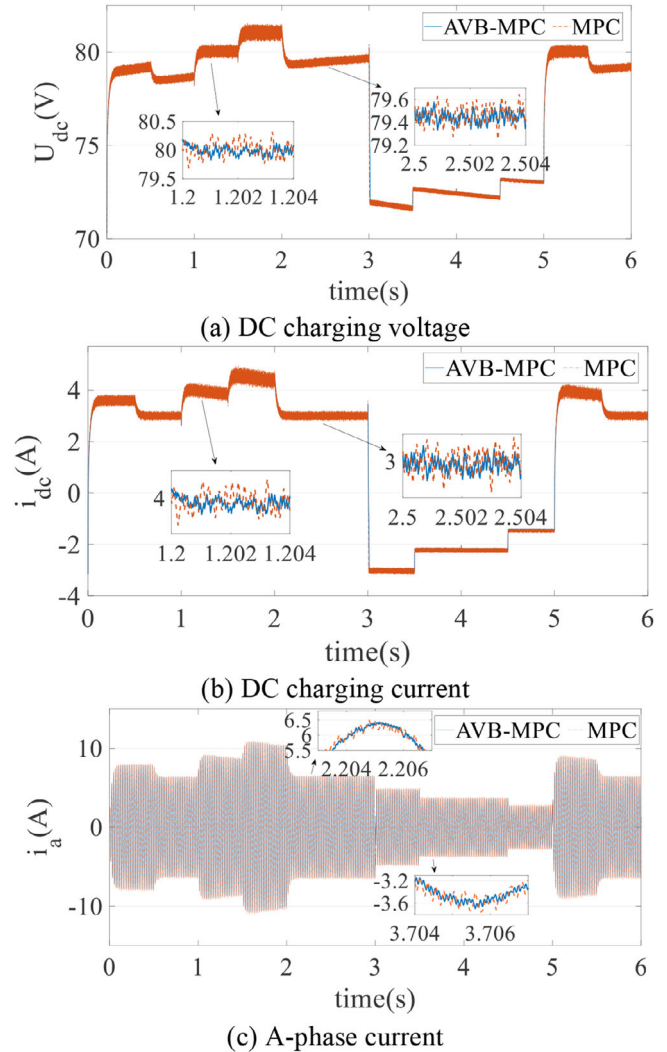
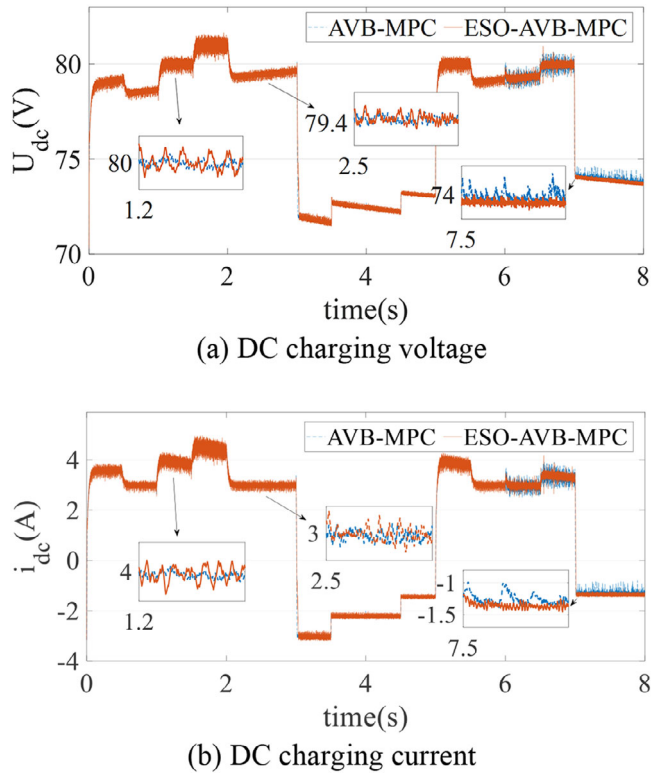
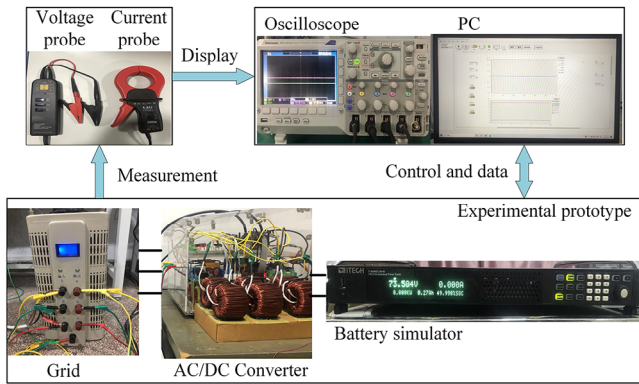


FIGURE 5 Comparative simulation results of AVB-MPC and MPC.



**FIGURE 6** Comparative simulation results of AVB-MPC and ESO-AVB-MPC.



**FIGURE 7** Experimental setup of EV battery charging and discharging system.

The control block diagram for the AVB-MPC based on ESO (ESO-AVB-MPC) is shown in Figure 4. The Charging/Discharging Mode block determines the battery state and generates the inner control loop reference current.

## 4 | SIMULATION VERIFICATION

A simulation model for EV battery charging and discharging is built to verify the proposed methods. The simulation parameters are given in Table 2. The test conditions are shown in Table 3.

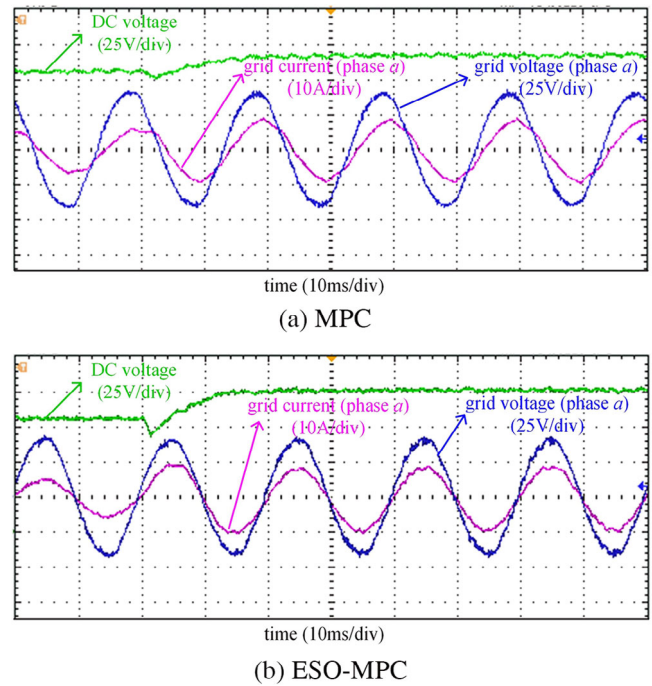


**FIGURE 8** Comparative experimental waveform between MPC and ESO-MPC when model parameters are inaccurate ( $L = 2$  mH in the algorithm).

**TABLE 2** System parameters.

Parameters	Values
Source phase voltage RMS $e$ (V)	30
Inductance $L$ (mH)	12.2
Resistance $R$ ( $\Omega$ )	0.5
DC capacitance $C$ ( $\mu$ F)	1000
DC voltage (V)	80-100
Threshold $C_b$	0.01
Sampling time $T_s$ ( $\mu$ s)	100

The comparative results between the AVB-MPC and MPC are shown in Figure 5.

As can be seen from Figure 6a,b, the ripples of DC charging voltage and current in AVB-MPC are smaller than that of traditional MPC. In addition, it can be seen from the comparison waveform of A-phase current shown in Figure 6c and the data in Table 3, that the current harmonic content of AVB-MPC is significantly lower than that of traditional MPC. The simulation results demonstrate that the AVB-MPC shows an improved overall control performance.

The comparative results between AVB-MPC and ESO-AVB-MPC are shown in Figure 6. In order to simulate the inaccurate parameters, the system parameters were changed at 6 s ( $R$  from 0.5 to 0.05  $\Omega$ ,  $L$  from 12.2 to 2 mH).

As shown in Figure 6, when the parameters are accurate (during 0–6 s), the control performance of AVB-MPC and ESO-AVB-MPC is similar. In addition, the data in Table 3 also

**TABLE 3** Comparative simulation results between MPC, AVB-MPC, and ESO-AVB-MPC.

Time (s)	EV battery state	Control mode	Control command	MPC		AVB-MPC		ESO-AVB-MPC	
				Fundamental (A)	THD (%)	Fundamental (A)	THD (%)	Fundamental (A)	THD (%)
0–0.5	Charging	Constant current	3.6 A	7.791	1.94	7.759	1.05	7.754	1.53
0.5–1			3 A	6.26	2.35	6.232	1.24	6.23	1.76
1–1.5		Constant voltage	80 V	N/A					
1.5–2			81 V	N/A					
2–3		Constant current	3 A	6.336	2.38	6.314	1.26	6.316	1.81
3–3.5			Discharging	PQ control	200 W 10 Var	4.726	2.96	4.702	1.5
3.5–4	150 W 30 Var	3.605			3.77	3.596	1.93	3.619	2.45
4–4.5			150 W –20 Var	3.588	3.77	3.564	1.92	3.569	2.47
4.5–5			100 W 50 Var	2.646	5.41	2.626	2.63	2.631	3.13
5–5.5	Charging	Constant voltage	80 V	N/A					
5.5–6			Constant current	3 A	6.312	2.43	6.289	1.22	6.28
6–6.5	3 A	N/A			5.665	9.52	5.656	4.31	
6.5–7		Constant voltage	80 V	N/A					
7–8			Discharging	PQ control	100 W 50 Var	N/A		2.53	18.48

**TABLE 4** Comparative Experimental Results between MPC, AVB-MPC and ESO-AVB-MPC when Model Parameters Are Accurate.

Test stage	EV battery state	Control mode	Control command	MPC		AVB-MPC		ESO-AVB-MPC	
				Fundamental (A)	THD (%)	Fundamental (A)	THD (%)	Fundamental (A)	THD (%)
1	Charging	Constant current	2 A	4.917	6.68	4.883	5.46	4.808	5.85
2			3 A	8.623	5.33	8.455	4.17	8.321	4.04
3		Constant voltage	80 V	N/A					
4			86 V	N/A					
5		Constant current	2.5 A	6.686	5.28	6.549	4.2	6.439	4.47
6			Discharging	PQ control	90 W 30 Var	2.469	12.85	2.541	8.17
7	120 W 30 Var	3.008			9.6	3.062	7.23	2.833	8.52
8	Charging	Constant current	2.5 A	6.669	5.47	6.523	4.01	6.426	4.45
9	Discharging	PQ control	120 W 30 Var	3.016	9.94	3.082	6.88	2.848	8.63
10	Charging	Constant voltage	83 V	N/A					

shows that AVB-MPC and ESO-AVB-MPC have similar performance. However, when the parameters are inaccurate (during 6–8 s), it is evident from Figure 6 and Table 3 that the ripples of DC charging voltage and current in ESO-AVB-MPC are smaller than that of the AVB-MPC. These results verify the robustness of ESO-AVB-MPC against the parameter inaccuracy. It is worth mentioning that the more inaccurate the model parameters, the worse the control performance. According to the simulation results, the control performance is still satisfactory when the inductance inaccuracy reaches about 83%, i.e. a discrepancy of 10.2 mH.

## 5 | EXPERIMENTAL VERIFICATION

In order to verify the simulation results, a battery charging and discharging control experimental platform based on a three-phase bridge fully-controlled rectifier and an EV battery simulator is built, as shown in Figure 7. The experimental parameters are consistent with the simulation parameters given in Table 2.

Firstly, the ESO-MPC is tested. In order to simulate the scenario where the parameters are inaccurate, the inductance  $L$  in the algorithm is set to 2 mH while the real value is 12.2 mH. The comparative results between the traditional MPC and the ESO-MPC are shown in Figure 8.

It can be seen from Figure 8a that the traditional MPC cannot provide satisfactory performance when the parameter is inaccurate. When the DC voltage reference changes from 80 to 100 V, the traditional MPC cannot effectively regulate the DC voltage to follow the reference and an obvious steady-state error as observed in Figure 8a. In addition, neither the grid current can be effectively controlled to be in phase with the grid voltage for a unity power factor operation. However, both the DC voltage and grid current (thus input power factor) can be effectively controlled with the ESO-MPC even when the system parameter is not accurately known, as shown in Figure 8b. The DC voltage is regulated to track the reference and the grid current is in phase with the grid voltage. The results in Figure 8 demonstrate the strong robustness of the ESO-MPC to the parameter inaccuracy or mismatch.

Secondly, in order to demonstrate the feasibility and effectiveness of the AVB-MPC strategy, a comparative experimental test with the conventional MPC under different charging and discharging conditions is carried out and results are shown in Figure 9. The experimental test conditions including ten test stages and corresponding data are given in Table 4.

As observed from Figure 9, both the traditional MPC and the AVB-MPC can effectively control the EV converter under different charging and discharging conditions. As seen in EV battery voltage and current waveforms in Figures 9c and 9d, the AVB-MPC offers lower ripples. In addition, the AVB-MPC exhibits lower fundamental current values (thus higher efficiency) and noticeably lower total harmonic distortions (THD) of the grid current under various conditions, as seen in Table 4. The execution time of the AVB-MPC strategy is 81  $\mu$ s, and it is similar to the traditional MPC (76  $\mu$ s). Experimental results vali-

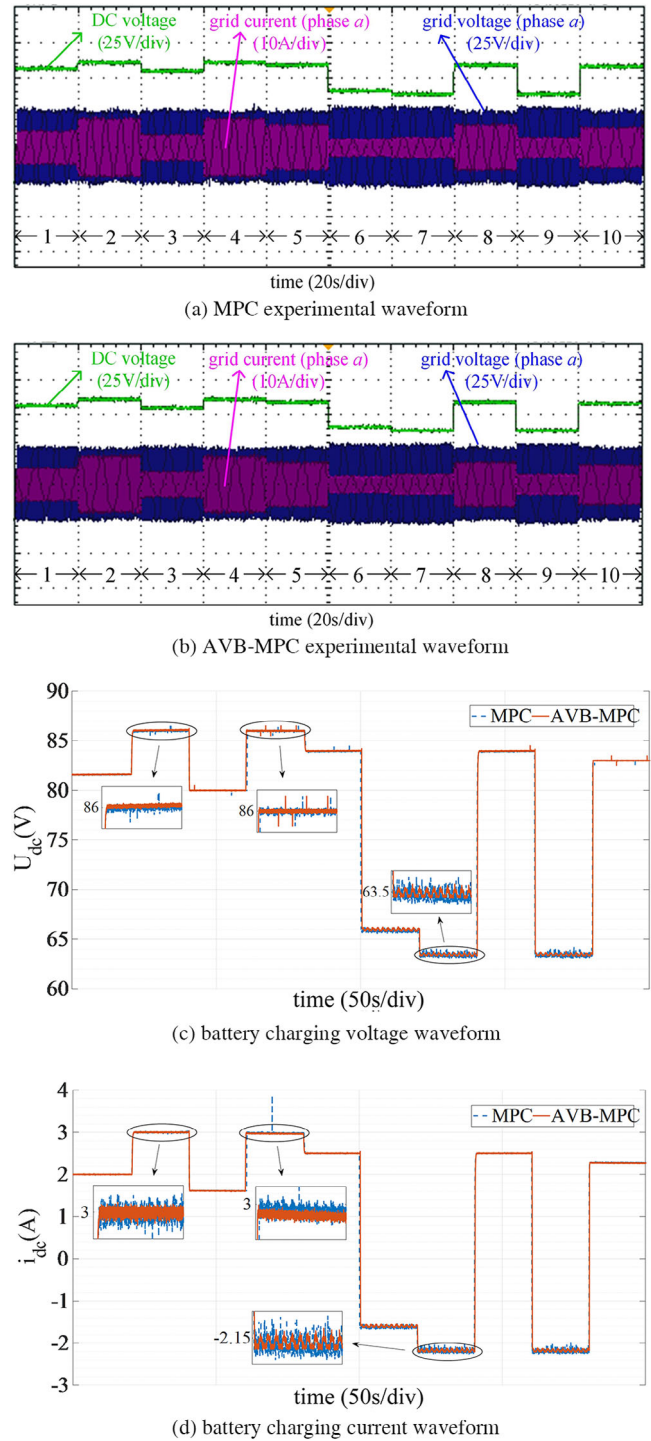


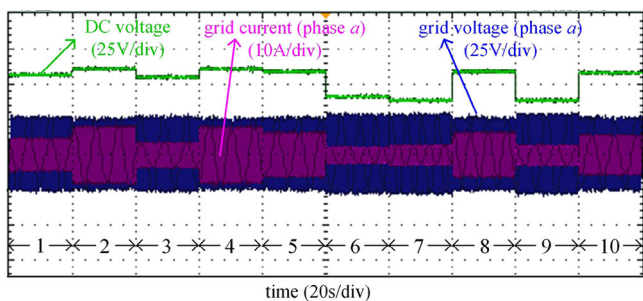
**FIGURE 9** Comparative experimental results between MPC and AVB-MPC.

date that the AVB-MPC strategy provides better overall control performance and a low computational burden is maintained.

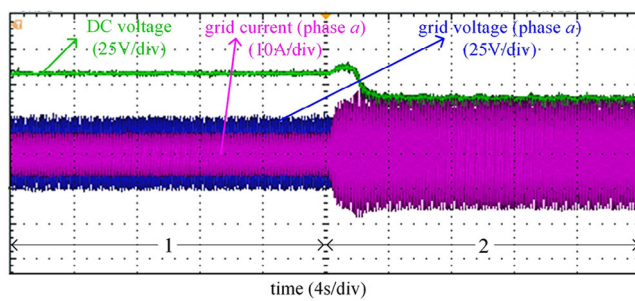
Finally, the proposed ESO-AVB-MPC has been experimentally verified. The comparative experimental results between AVB-MPC and ESO-AVB-MPC, when parameters are accurately known, are shown in Figure 10. As shown in Figure 10, both the AVB-MPC and ESO-AVB-MPC methods show sat-

**TABLE 5** Comparative experimental results of AVB-MPC and ESO-AVB-MPC when model parameters are inaccurate.

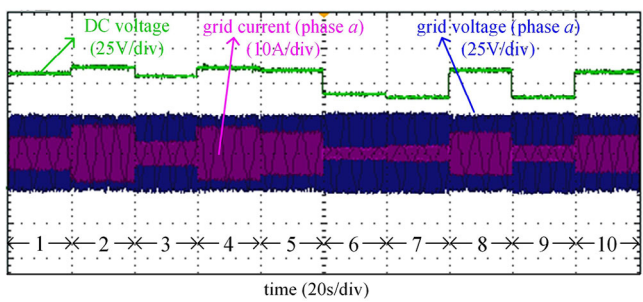
Test stage	Battery state	Control mode	Control command	AVB-MPC	ESO-AVB-MPC
1	Charging	Constant current	2 A	≈2 A	≈2 A
2			3 A	Unsatisfactory	≈3 A
3			80 V	≈80 V	
4	Discharging	PQ control	86 V	≈86 V	≈86 V
5			2.5 A	≈2.5 A	≈2.5 A
6			90 W 30 Var	≈90 W ≈30 Var	
7	Charging	Constant current	120 W 30 Var	≈120 W ≈30 Var	≈120 W ≈30 Var
8			2.5 A	≈2.5 A	
9			120 W 30 Var	≈120 W ≈30 Var	
10	Charging	Constant voltage	83 V	≈83 V	≈83 V



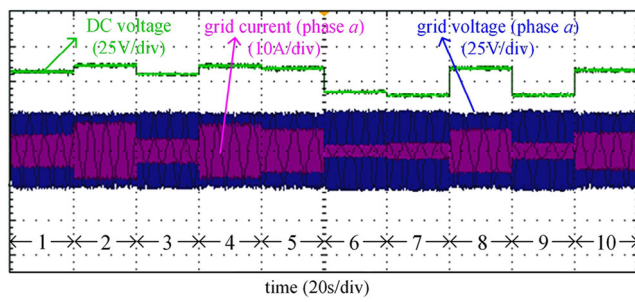
(a) AVB-MPC



(a) AVB-MPC



(b) ESO-AVB-MPC



(b) ESO-AVB-MPC

**FIGURE 10** Comparative experimental results of AVB-MPC and ESO-AVB-MPC when model parameters are accurate.

**FIGURE 11** Comparative experimental results of AVB-MPC and ESO-AVB-MPC when model parameters are inaccurate.

isfactory control performance under different test conditions where the parameters are accurate. The experimental data in Table 4 also show that both methods have relatively similar performances in regulating EV battery charging and discharging. The THDs in experimental results are higher than the simulation results because the three-phase voltage source is from a non-ideal autotransformer, and its output voltage is easily influenced by the load.

However, when the system model parameters are inaccurate ( $L = 2 \text{ mH}$  and  $R = 0.05 \Omega$  in the algorithm), the AVB-MPC method cannot effectively regulate the system any longer, as

observed in the comparative results shown in Figure 11 and Table 5.

It can be seen from Figure 11a that when the charging current reference changes from 2 to 3 A, the AVB-MPC cannot achieve the control objective and the system is in an uncontrolled state due to the mismatch of system parameters. In contrast, the ESO-AVB-MPC strategy can still effectively regulate the EV charging converter under various conditions, even when the system parameters are inaccurate, as seen in Figure 11b. The above experimental results illustrate that the proposed ESO-AVB-MPC has stronger robustness to the parameter inaccuracy.

## 6 | CONCLUSION

This paper describes an adjacent vector-based model predictive control, which utilizes a predefined vector selection table based on the principles of using adjacent vectors and minimum switching actions. A control error threshold is introduced in the adjacent vector-based model predictive control to coordinate the use of 1-vector, 2-vector, and 3-vector MPC schemes, so the control accuracy can be improved without causing a noticeable increase in computational burden. Secondly, in order to enhance the robustness of adjacent vector-based model predictive control, a disturbance-rejection MPC based on the extended state observer has been investigated, in which the parameter inaccuracy is regarded as part of the system disturbance and is estimated by the extended state observer. The proposed schemes are experimentally validated on an EV converter charging and discharging control platform. The proposed methods can be readily extended to the control of other power electronic converters. Further studies can be carried out to improve the proposed methods, such as the study on the rigorous design of the threshold.

### AUTHOR CONTRIBUTIONS

**Jianwei Zhang:** Conceptualization; formal analysis; funding acquisition; investigation; resources; supervision; writing—review and editing. **Qiaosen Cao:** Formal analysis; investigation; software; validation; writing—original draft. **Guangchen Liu:** Project administration; resources; supervision; writing—review and editing. **Marco Rivera:** Project administration; resources; supervision; writing—review and editing. **Patrick Wheeler:** Project administration; resources; supervision; writing—review and editing.

### ACKNOWLEDGEMENTS

This work was supported in part by the Inner Mongolia Natural Science Foundation (2024MS05041), Program for Young Talents of Science and Technology in Universities of Inner Mongolia Autonomous Region (NJYT22082), Basic Scientific Research Expenses Program of Universities directly under Inner Mongolia Autonomous Region (JY20220092, JY20230009), China Scholarship Council (File No. 202208155013), and the University of Nottingham International Research Collaboration Fund (Project Code A71502), Fondecyt Regular Project (1220556), Anid/Anillo Project (ATE220023), FONDAP SERC Chile (1522A0006), and Inner Mongolia Autonomous Region Science and Technology Breakthrough Project: 2024KJTW0017.

### CONFLICT OF INTEREST STATEMENT

The authors declare no conflicts of interests.

### DATA AVAILABILITY STATEMENT

Data sharing is not applicable to this article as no new data were created or analysed in this study.

### ORCID

Jianwei Zhang  <https://orcid.org/0000-0001-5304-6297>

## REFERENCES

- Zhang, H., Tao, R., Li, Z., Zhang, X., Ma, Z.: Multivariable sequential model predictive control of LCL-type grid connected inverter. *IET Power Electron.* 16, 558–574 (2023). <https://doi.org/10.1049/pe12.12408>
- Vazquez, S., Rodriguez, J., Rivera, M., Franquelo, L.G., Norambuena, M.: Model predictive control for power converters and drives: Advances and trends. *IEEE Trans. Ind. Electron.* 64(2), 935–947 (2017). <https://doi.org/10.1109/TIE.2016.2625238>
- Karamanakos, P., Liegmann, E., Geyer, T., Kennel, R.: Model predictive control of power electronic systems: methods, results, and challenges. *IEEE Open J. Ind. Appl.* 1, 95–114 (2020). <https://doi.org/10.1109/OJIA.2020.3020184>
- An, X., Liu, Z., Chen, Q., Liu, G.: Robust virtual-vector model predictive control of permanent-magnet motor considering D-Q axis inductance parameter uncertainty. *IET Electr. Power Appl.* 18, 1–14 (2023). <https://doi.org/10.1049/elp2.12368>
- Saeed, M.S.R., Song, W., Huang, L., Yu, B.: Double-vector-based finite control set model predictive control for five-phase pmsms with high tracking accuracy and DC-link voltage utilization. *IEEE Trans. Power Electron.* 37(12), 15234–15244 (2022). <https://doi.org/10.1109/TPEL.2022.3188578>
- Zhang, X., Tao, R., Dou, Z., Qiu, S., Liu, J., Liu, Y.: Fast two-vector-based model-free predictive current control of permanent magnet synchronous motor. *IET Electr. Power Appl.* 17(2), 217–231 (2023). <https://doi.org/10.1049/elp2.12257>
- Guo, L., Chen, M., Li, Y., Wang, P., Jin, N., Wu, J.: Hybrid multi-vector modulated model predictive control strategy for voltage source inverters based on a new visualization analysis method. *IEEE Trans. Transport. Electric.* 9(1), 8–21 (2023). <https://doi.org/10.1109/TTE.2022.3161583>
- Zhang, Y., Xu, D., Huang, L.: Generalized multiple-vector-based model predictive control for PMSM drives. *IEEE Trans. Ind. Electron.* 65(12), 9356–9366 (2018). <https://doi.org/10.1109/TIE.2018.2813994>
- Parvathy, M.L., Kusuma, E., Thippiripati, V.K.: A modified duty-modulated predictive current control for permanent magnet synchronous motor drive. *IET Electr. Power Appl.* 15, 25–38. <https://doi.org/10.1049/elp2.12004>
- Harbi, I., Ahmed, M., Hackl, C.M., Rodriguez, J., Kennel, R., Abdelrahman, M.: Low-complexity dual-vector model predictive control for single-phase nine-level ANPC-based converter. *IEEE Trans. Power Electron.* 38(3), 2956–2971 (2023). <https://doi.org/10.1109/TPEL.2022.3218742>
- Yang, Y., Pan, J., Wen, H., Zhang, Z., Ke, Z., Xu, L.: Double-vector model predictive control for single-phase five-level actively clamped converters. *IEEE Trans. Transp. Electr.* 5(4), 1202–1213 (2019). <https://doi.org/10.1109/TTE.2019.2950510>
- Kang, S.-W., Soh, J.-H., Kim, R.-Y.: Symmetrical three-vector-based model predictive control with deadbeat solution for IPMSM in rotating reference frame. *IEEE Trans. Ind. Electron.* 67(1), 159–168 (2020). <https://doi.org/10.1109/TIE.2018.2890490>
- Li, H., Lin, M., Yin, M., Ai, J., Le, W.: Three-vector-based low-complexity model predictive direct power control strategy for PWM rectifier without voltage sensors. *IEEE J. Emerging Sel. Top. Power Electron.* 7(1), 240–251 (2019). <https://doi.org/10.1109/JESTPE.2018.2871332>
- Zhang, Y., Liu, J., Yang, H., Fan, S.: New insights into model predictive control for three-phase power converters. *IEEE Trans. Ind. Appl.* 55(2), 1973–1982 (2019). <https://doi.org/10.1109/TIA.2018.2873505>
- Chen, Z., Qiu, J.: Adjacent-vector-based model predictive control for permanent magnet synchronous motors with full model estimation. *IEEE J. Emerging Sel. Top. Power Electron.* 11(2), 1317–1331 (2023). <https://doi.org/10.1109/JESTPE.2022.3172714>
- Zhang, Y., Wang, X., Yang, H., Zhang, B., Rodriguez, J.: Robust predictive current control of induction motors based on linear extended state observer. *Chin. J. Electr. Eng.* 7(1), 94–105 (2021). <https://doi.org/10.23919/CJEE.2021.000009>
- Rodriguez, J., et al.: Latest advances of model predictive control in electrical drives—part I: basic concepts and advanced strategies. *IEEE Trans. Power Electron.* 37(4), 3927–3942 (2022). <https://doi.org/10.1109/TPEL.2021.3121532>

18. Khalilzadeh, M., Vaez-Zadeh, S., Rodriguez, J., Heydari, R.: Model-free predictive control of motor drives and power converters: a review. *IEEE Access* 9, 105733–105747 (2021). <https://doi.org/10.1109/ACCESS.2021.3098946>
19. Liu, X., et al.: Event-triggered ESO-based robust MPC for power converters. *IEEE Trans. Ind. Electron.* 70(2), 2144–2152 (2023). <https://doi.org/10.1109/TIE.2022.3167135>
20. Huang, D., Fang, S., Pan, Z., Wang, Y.: Low-speed model predictive control based on modified extended state observer of arc motor. *IEEE Trans. Ind. Electron.* 70(7), 6675–6685 (2023). <https://doi.org/10.1109/TIE.2022.3203681>
21. Zhang, Y., Jin, J., Huang, L.: Model-free predictive current control of PMSM drives based on extended state observer using ultralocal model. *IEEE Trans. Ind. Electron.* 68(2), 993–1003 (2021). <https://doi.org/10.1109/TIE.2020.2970660>
22. Liu, H., Lin, W., Liu, Z., Buccella, C., Cecati, C.: Model predictive current control with model-aid extended state observer compensation for PMSM drive. *IEEE Trans. Power Electron.* 38(3), 3152–3162 (2023). <https://doi.org/10.1109/TPEL.2022.3225626>
23. Han, J.: From PID to active disturbance rejection control. *IEEE Trans. Ind. Electron.* 56(3), 900–906 (2009). <https://doi.org/10.1109/TIE.2008.2011621>
24. Zhang, J., Tian, G., Liu, G.: Active disturbance rejection decoupling control of grid-connected PWM converter. In: 2022 4th International Conference on Power and Energy Technology (ICPET), pp. 1215–1220. IEEE, Piscataway, NJ (2022). <https://doi.org/10.1109/ICPET55165.2022.9918484>

**How to cite this article:** Zhang, J., Cao, Q., Liu, G., Rivera, M., Wheeler, P.: Disturbance-rejection adjacent vector model predictive control strategy based on extended state observer for EV converter. *IET Power Electron.* 17, 2572–2583 (2024). <https://doi.org/10.1049/pel2.12807>